

A study on storm surge sensitivity to tropical cyclone intensification and translation speed variation at the southeastern coast of South Korea

Yeongseok Jeong

Abstract:

This study investigates the sensitivity of storm surge heights along the southeastern coast of the Korean Peninsula to tropical cyclone (TC) intensification under varying translation speeds, represented by MPN (-10%), MPO (baseline), and MPP ($+10\%$). Simulations show that intensified TCs consistently generate higher peak storm surges than observed values at Busan, Masan, and Ulsan, with Masan exhibiting the largest surges across all events due to its semi-enclosed bay geometry. Among the scenarios, MPO generally produces the highest peak surge heights, although localized exceptions occur, indicating non-linear surge responses to translation speed changes. Differences in peak surge heights among translation speed scenarios range from 2.1% to 12.2% , reflecting complex interactions among storm intensity, track, duration, and coastal configuration. These findings highlight the pronounced vulnerability of Masan to TC intensification and underscore the necessity of site-specific storm surge assessments under future climate conditions.

1. Introduction

Storm surge is an abnormal rise of sea levels above astronomical tides by a storm (NHC 2014c), and it poses significant flooding threats to coastal areas across the world (Wahl et al. 2015; Fang et al. 2021; Karim et al. 2008; Terenzi et al. 2014; Hoshino et al. 2016). Since storm surge is developed on top of climate change-induced sea level rise (SLR), the reoccurrence interval of more destructive storm surge-induced flooding is likely to decrease in the future (Lin et al. 2012). Moreover, anthropogenic global warming is responsible for tropical cyclone (TC) identification (Knutson et al. 2020), highlighting the need for projecting storm surge variability accordingly.

Climatologically, three to four TCs on average in every year directly/indirectly affect the Korean Peninsula (KP) (Kim et al. 2019), and associated hazards have resulted in significant economic loss. For example, the average economic damage of TCs that affected KP is approximately ₩186 billion won (\$126 million USD), and TC MAEMI (2003), in particular, caused over 60,000 displaced people and nearly ₩5.87 trillion won (\$4 billion USD) in property damage (Kim et al. 2015). Specifically, low-lying areas, such as Ulsan, Masan, and Busan, on the southeastern coast (SEC) of KP, where numerous TCs make landfall, have been showing high vulnerability to flooding threats (Yoo et al. 2013; Gyu et al. 2015; Choi et al. 2024), and this trend is expected to be exacerbated due to climate warming and SLR (Kim et al. 2017; Kim et al. 2023).

Studies on storm surge impact around KP have been widely conducted by previous research. For example, Kim et al. (2017) showed that there has

been an increasing trend in annual maximum surge height at SEC, which indicates 1.48 to 3.71 mm per year, representing that the trend was largely attributable to TCs. Jin et al. (2024) performed numerical simulations of storm surge with diverse TC intensification scenarios, identifying storm surge sensitivity around KP. Generating synthetic TCs and assessing potential storm surge hazards at the west coast of KP have been addressed by Kim et al. (2025), and they adopted a comprehensive approach to the evaluation of storm surge response, including meteorological factors, distance from mainland, and dynamic interaction with geographical features. However, a statistical approach to the enhancement of TC intensity as well as investigating storm surge variability using downscaled meteorological forcing around KP have not been documented. Furthermore, little is known about the effect of TC translation speed variations on storm surge risks at coastal areas in KP.

In this study I aim to quantitatively examine the response of storm surge height to the variability of TCs intensity and translation speed at low-lying coastal regions in SEC of South Korea. To ensure reliability as well as conservativeness in this research, I conduct high-resolution numerical modeling of meteorological forcing and storm surge based on three historical maximum TCs, MAEMI (2003), MAYSAK (2009), and HINNAMNOR (2022) (Figure 1). Astronomical tides are not considered for the accurate and isolated evaluation on storm surge sensitivity.

2. Data and Methods

a. Tropical cyclone variability

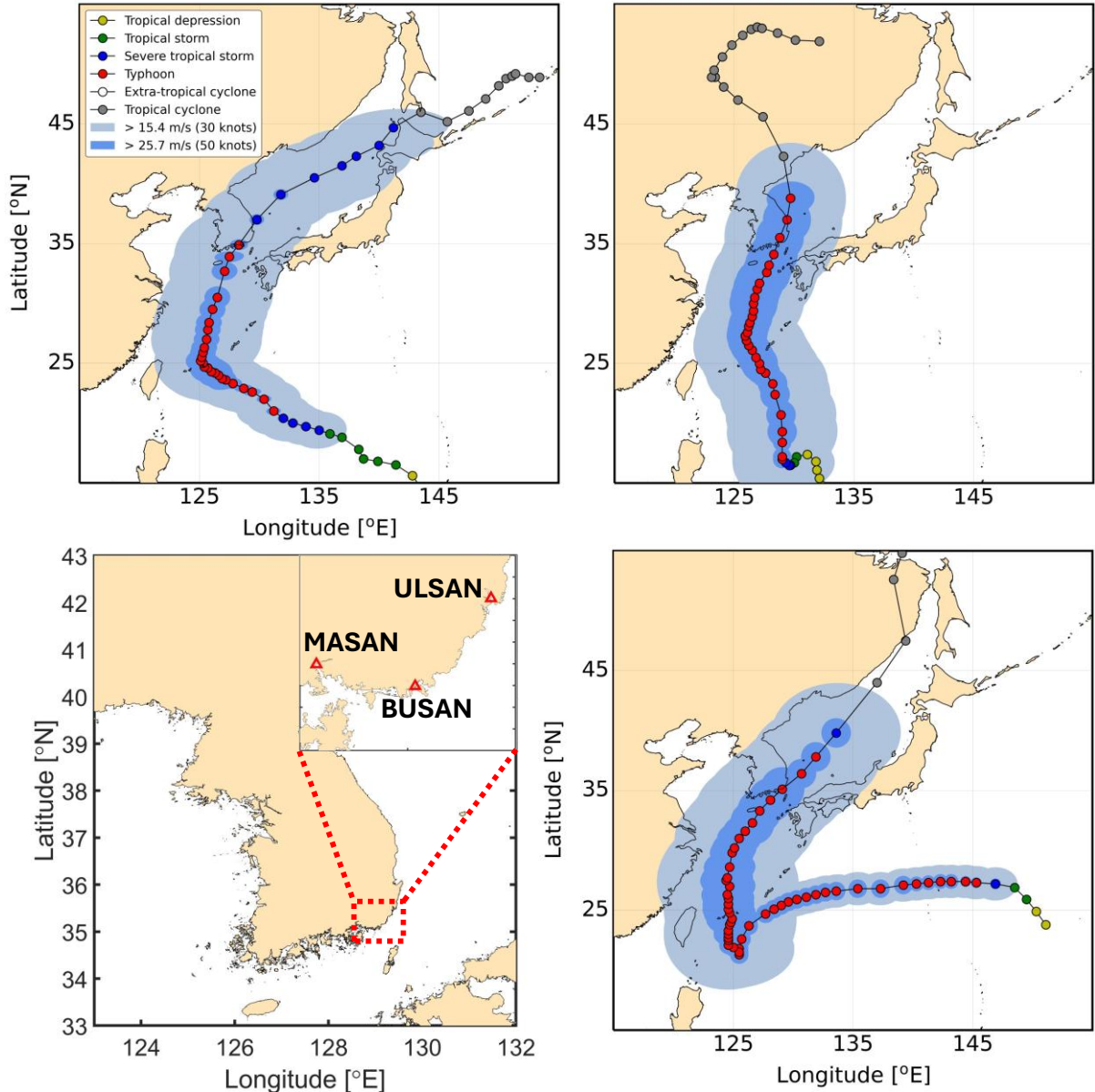


Figure 1. Tracks of three historical maximum tropical cyclones, MAEMI (2003), MAYSAK (2009), and HINNAMNOR (2022), are depicted on the upper left, on the upper right, and on the lower right panel, respectively. Intensity evolution and radius of wind speeds are displayed based on RSMC best track datasets. The lower left panel represents three target locations for this study in SEC.

Recognizing the report suggested by Knutson et al. (2020) that the lifetime maximum wind speeds of tropical cyclones will be enhanced about 5% as global warming continues to increase by 2°C, I examine global near surface air temperature anomaly projections depending on climate scenarios by taking ensemble average of 17 members in CMIP6 climate models (Figure 2). To represent the most severe case, the SSP5-8.5 scenario is considered for this study. To encompass problem TCs in climatological shifts, the reference year to is set to 2022. By 2100, global mean near surface air temperature anomaly

is projected to reach 5.415°C, compared with 0.937°C in 2022. Therefore, the difference corresponds to an approximately 11.2% increase in intensity.

Moreover, in order to simulate tropical cyclone climatological shifts as a function of increasing return periods, this study conducts extreme value analysis on annual maximum wind speed of synthetic tropical cyclones from Synthetic Tropical cyclOne geneRation Model (STORM) datasets (Bloemendaal et al. 2020). Leveraging the model's capability that statistically extrapolates

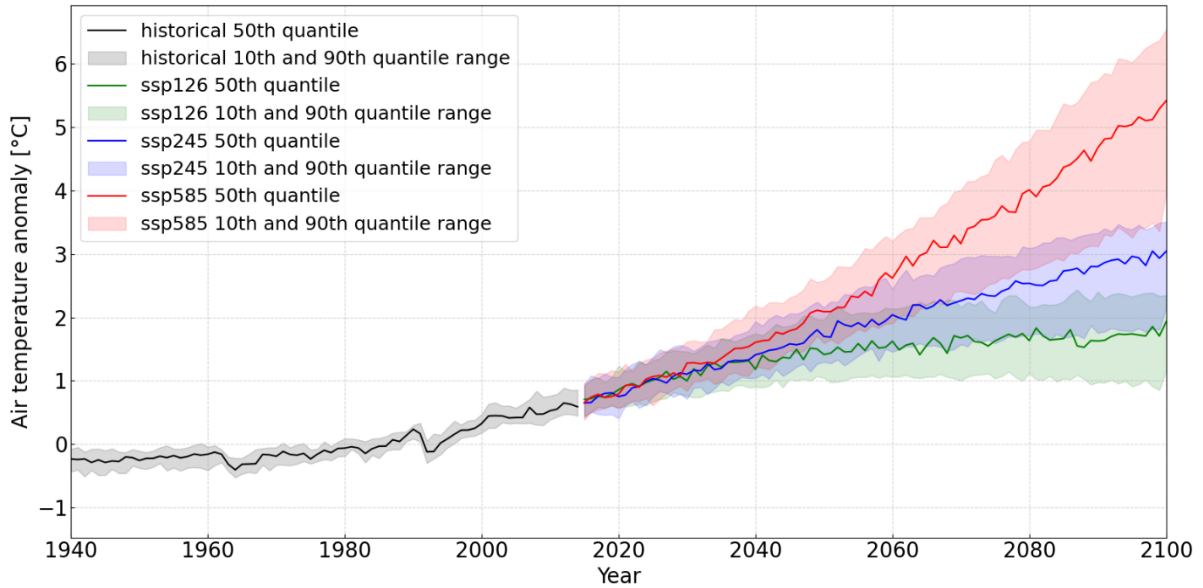


Figure 2. Ensemble averaged global near surface air temperature anomaly projections from 17 CMIP6 climate models. Anomalies were referenced on 1940–2015.

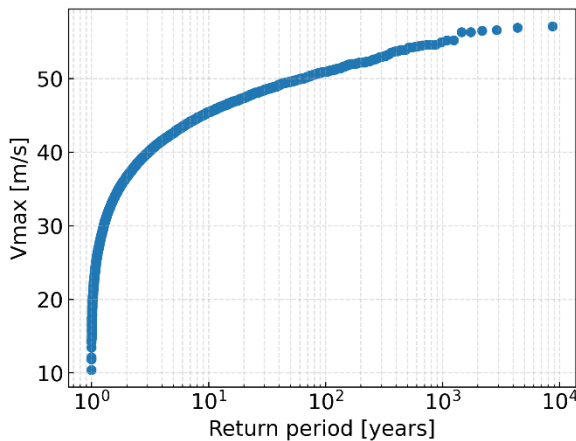


Figure 3. Estimated return periods of annual maximum wind speed over the study domain

beyond the limited historical best track datasets, I generate a total of 214,863 synthetic tropical cyclones from 4164 historical tropical cyclones recorded in the International Best Track Archive for Climate Stewardship (IBTrACS) (Knapp et al. 2010) datasets during 1842–2024. From these, 20,894 storms are specifically selected based on whether their track enters the domain (120°E – 130°E , 28°N – 33°N), a region in which the majority of historical tropical cyclones that affected South Korea experience their lifetime maximum intensity. I then fit a Generalized Extreme Value (GEV) distribution to the annual maximum wind speeds over the domain and estimate the 1,000-year return period maximum wind speed (Figure 3). Since MAYSAK (2009)

exhibits the highest wind speed within the domain (52.3 m s^{-1}) and 1000-year return level maximum wind speed is 57.1 m s^{-1} , the corresponding intensity increases for return period-based analysis are estimated to be 9.2%.

Lastly, the influence of tropical cyclone translation speed on storm surge mobilization has been well documented (Rego et al. 2009; Irish et al. 2008), reporting that faster translation speeds result in higher storm surge peak heights. Due to the complex geographical configurations around South Korea, however, the resulting pattern may differ from those reported in previous studies, and this highlights the need to identify research consistency within the domain of this study. In this regard, variations in translation speed are imposed using an arbitrarily chosen $\pm 10\%$ adjustment, and these sensitivity tests are included in the analysis.

The final intensity increase is set to 21.4%, and additional variations in translational speed yielded a total of three distinct experiments for each TC. I name each experiment scenario as MPN, MPO, and MPP, which indicate Maximum Probable case with Negative translation speed modification, Original, and Positive translation speed modification, respectively.

(b) Atmospheric forcing

Dynamic downscaling of TC meteorological fields using the Weather Research and Forecasting Model v4.3.1 (WRF) (Skamarock et al. 2019) is

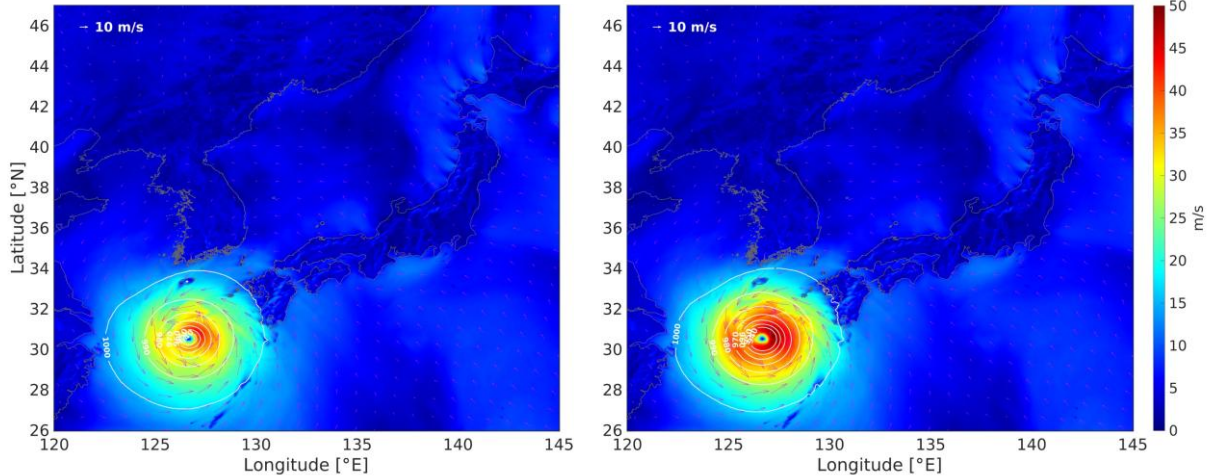


Figure 4. Downscaled meteorological fields of TC MAYSAK (2020). Left and right panels show the original and intensified case. Color shading and quivers represent wind speed and direction.

conducted. For atmospheric boundary conditions, I use the Japan Meteorological Agency’s Global Spectrum Model (JMA-GSM) with 0.125° horizontal resolution. Because no suitable datasets are available prior to 2005, the NCEP/NCAR Reanalysis 1 with 0.5° horizontal resolution is used to force simulations of TC MAEMI (2003). For the regional domain encompassing Korea and Japan, the Japan Meteorological Agency Mesoscale Model (JMA-MSM) fields at 0.05° spatial resolution are merged with the global-scale atmospheric fields to render high-resolution representations of TC structures. Sea surface temperature inputs are primarily derived from NCEP-CFSv2, but NCEP-CFSR is employed for experiments in TC MAEMI (2003) considering data availability. Physical parameterization schemes and further setting information are described in Table 1.

The meteorological fields of TCs can be expressed as the sum of the environmental component (F^E) and the rotational component (F^V), as shown in Equation (1). The rotational component is isolated within the TC’s area of influence, defined by the radius of 30-knot (R30) using the vortex separation method presented by Nguyen and Chen (2011) and I apply the intensification factor to F^V .

$$F = F^V + F^E \quad (1)$$

The method is an improved adaptation of the technique originally introduced by Kurihara et al. (1993) for application to high-resolution meteorological fields. In order to extract F^V , I follow the separation procedure of F^E from the total field (F) as presented in Equation (2) and (3).

$$\overline{F_{i,j}^E} = F_{i,j} + K_m(F_{i-q_n,j} + F_{i+q_n,j} - 2F_{i,j}) \quad (2)$$

$$F_{i,j}^E = \overline{F_{i,j}^E} + K_m\left(\overline{F_{i,j-q_n}^E} + \overline{F_{i,j+q_n}^E} - 2\overline{F_{i,j}^E}\right) \quad (3)$$

, where i and j denote x and y grid points,

$$q_n = \left[\frac{111 \cos(\phi_0)}{n \Delta} \right], n = 1, 2, 3, \dots, M$$

$$M = \left[\frac{111 \cos(\phi_0)}{\Delta} \right]$$

$$K_m = \left[\frac{1}{2} \left(1 - \cos \frac{2\pi}{m} \right)^{-1} \right] \\ , m = 2, 3, 4, 2, 5, 6, 7, 2, 8, 9, 2$$

This work is automated by an NCL script and performed for each hourly meteorological input.

Table 1. WRF model setup

Maps and grids	
Total # of grids	720,000 (800×900)
Calculation domain	$105^\circ\text{E}-155^\circ\text{E}$ ($3,600$ km) $10^\circ\text{N}-49^\circ\text{N}$ ($4,050$ km)
Grid spacing	4.5 km
Vertical levels	30
Projection	Lambert-Conformal
Physical parameterization schemes	
Microphysics	WSM 6-class graupel scheme
Planetary Boundary Layer	YSU PBL scheme
Surface Layer	Revised MM5 Monin-Obukhov scheme
Longwave radiation	RRTMG scheme
Shortwave radiation	RRTMG scheme
Cumulus	A newer Tiedtke scheme
Land surface model	Thermal diffusion scheme

After the TC intensification process, I create additional scenarios with varying translation speed by 10% increment and decrement. Modified TC locations are linearly interpolated in time between consecutive output times, and associated physical properties are determined using time-normalized weights based on the distance of the target time from each neighboring time step as following in Equation (4).

$$X(t) \approx X(t_b) \cdot \frac{t_a - t}{t_a - t_b} + X(t_a) \cdot \frac{t - t_b}{t_a - t_b} \quad (4)$$

, where t_a and t_b represent the original timestep after and before the target timestep.

(c) Storm surge modeling

I employ the Advanced CIRCulation (ADCIRC) model (Luettich et al. 1992), which has been widely used for simulating coastal water levels, storm surge dynamics, and tide- and wind-driven circulation across a broad range of spatial scales (Westerink et al. 2008). ADCIRC uses finite element grids for its computational domain, and depth-integrated ADCIRC (ADCIRC-2DDI) is utilized for this study. Water level estimation is achieved through the main solution algorithm, which is the Generalized Wave Continuity Equation (GWCE) and momentum equations, as presented in Equation (5)-(7).

$$\begin{aligned} \frac{\partial^2 \zeta}{\partial t^2} + \tau_0 \frac{\partial \zeta}{\partial t} + S \frac{\partial A_x}{\partial x} + \frac{\partial A_y}{\partial y} - UHS \frac{\partial \tau_0}{\partial x} \\ - VH \frac{\partial \tau_0}{\partial y} - \frac{A_y \tan \phi}{R} = 0 \end{aligned} \quad (5)$$

$$\begin{aligned} \frac{\partial U}{\partial t} + SU \frac{\partial U}{\partial x} + V \frac{\partial U}{\partial y} - \left(\frac{U \tan \phi}{R} + f \right) V = \\ -S \frac{\partial}{\partial x} \left[\frac{p_s}{\rho_0} + g\zeta - g(\eta + \gamma) \right] + \frac{\tau_{sx}}{\rho_0 H} - \frac{\tau_{bx}}{\rho_0 H} + D_x - B_x \end{aligned} \quad (6)$$

$$\begin{aligned} \frac{\partial V}{\partial t} + SU \frac{\partial V}{\partial x} + V \frac{\partial V}{\partial y} - \left(\frac{U \tan \phi}{R} + f \right) U = \\ -S \frac{\partial}{\partial y} \left[\frac{p_s}{\rho_0} + g\zeta - g(\eta + \gamma) \right] + \frac{\tau_{sy}}{\rho_0 H} - \frac{\tau_{by}}{\rho_0 H} + D_y - B_y \end{aligned} \quad (7)$$

, where

$$x = R(\lambda - \lambda_0) \cos \phi_0$$

$$y = R\phi$$

$$\begin{aligned} A_x = U \frac{\partial H}{\partial t} + H \left\{ -US \frac{\partial U}{\partial x} - V \frac{\partial U}{\partial y} + fV \right. \\ \left. - S \frac{\partial}{\partial x} \left[\frac{p_s}{\rho_0} + g\zeta - g(\eta + \gamma) \right] + \frac{\tau_{sx}}{\rho_0 H} \right. \\ \left. - \frac{\tau_{bx}}{\rho_0 H} + D_x - B_x + \tau_0 U \right\} \end{aligned}$$

$$\begin{aligned} A_y &= V \frac{\partial H}{\partial t} + H \left\{ -US \frac{\partial V}{\partial x} - V \frac{\partial V}{\partial y} + fU \right. \\ &\quad \left. - \frac{\partial}{\partial y} \left[\frac{p_s}{\rho_0} + g\zeta - g(\eta + \gamma) \right] + \frac{\tau_{sy}}{\rho_0 H} \right. \\ &\quad \left. - \frac{\tau_{by}}{\rho_0 H} + D_y - B_y + \tau_0 V \right\} \\ H &= h + \zeta \\ S &= \frac{\cos \phi_0}{\cos \phi} \end{aligned}$$

ζ is free surface displacement, t is time, τ_0 is a weight to induce GWCE, λ and ϕ are longitude and latitude, λ_0 and ϕ_0 are reference longitude and latitude, R is Earth radius, U and V are vertically integrated current velocity for x and y direction, h is water depth, f is the Coriolis coefficient, p_s is sea level pressure, ρ_0 is water density, g is gravitational acceleration, η is tides, γ is load tide, τ_{sx} and τ_{sy} are wind shear stress in x and y direction, τ_{bx} and τ_{by} are bottom friction in x and y direction, D_x and D_y are momentum diffusion term in x and y direction, B_x and B_y are baroclinic pressure gradient term in x and y direction.

Ensuring adequate mesh quality is of great importance in maintaining computational stability. In this regard, I generate unstructured grids using the Surface-water Modeling System software and undergo repetitive mesh quality optimization to compromise accuracy in outcomes and stability in calculation. For the entire computational domain of 113.92°E-145.51°E and 17.97°N-52.09°N, the total number of nodes and elements are 423,304 and 224,736. Moreover, embedding high-resolution bathymetry information in the calculation domain facilitates reliable simulation of surge spatiotemporal distribution. Considering its significance, I use SRTM15+ v2.1 datasets with 15 arc seconds resolution for regional domain, and BADA v1.0 datasets (Yoo et al. 2019) with 5 arc seconds are utilized for local bathymetry around KP (Figure 5).

The performance of ADCIRC is validated through the direct comparison between calculated surge heights obtained from hindcasts and observed surge heights retrieved from the three tidal gauges that this study addresses. Since observed water level data contains astronomical tides, I use the Tidal Model Driver v3.0 to remove eight tidal components (M2, S2, K1, O1, N2, K2, P1, Q1). To further purify the observed data, I conduct Fast Fourier Transform and eliminate dominant

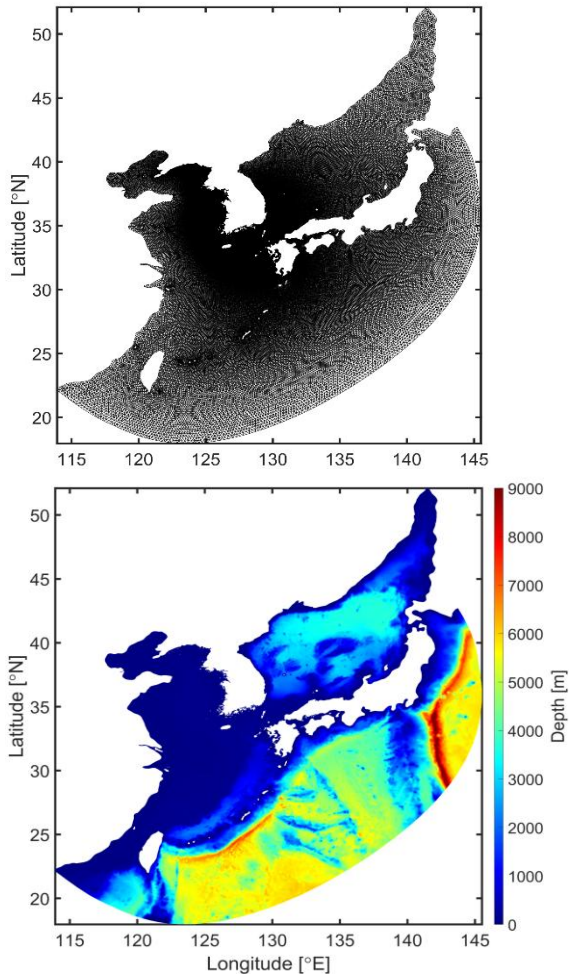


Figure 5. Finite element grids (top) and depth distribution (bottom) within storm surge calculation domain

sinusoidal waves. To verify statistical coherence between calculated and observed surge heights, I examine correlation coefficients and Root Mean Square Error (RMSE), as shown in Figure 6. Geographically, coastal areas in the Yellow Sea and the South Sea are susceptible to strong tidal effects, and this tendency becomes weaker in the East Sea, which is likely to play a key role in enhancing prediction uncertainties at the Masan tidal gauge due to residual tidal components regardless of thorough preliminary purification on observations.

3. Results

Table 2 summarizes the peak storm surge heights at Busan, Masan, and Ulsan associated with intensified tropical cyclones (TCs) under three translation speed variation scenarios (MPN, MPO, and MPP), along with observed (OBS) values. Overall, intensified TC scenarios consistently

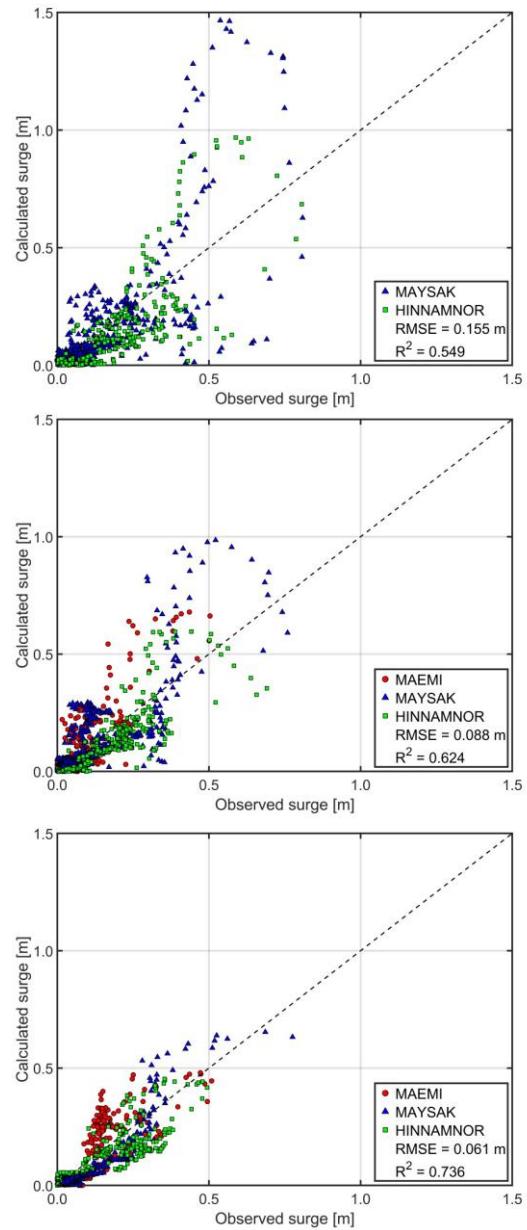


Figure 6. Validation results at three tidal gauges, Masan (top), Busan (middle), and Ulsan (bottom). Red circles, blue triangles, green squares indicate storm surge heights from MAEMI, MAYSAK, and HINNAMNOR, respectively. Observed surge heights from MAEMI at the Masan tidal gauge are omitted due to the absence of available data.

produce higher peak surge heights than observations across all tidal gauges and storm cases, indicating a strong sensitivity of coastal water levels to TC intensification.

For MAEMI (2003), peak surges at Masan range from 1.60 m (MPP) to 1.79 m (MPO), compared to 1.29 m in the observed data. Similar patterns are evident for MAYSAK (2009), where Masan

Table 2. Peak storm surge heights associated with intensified TCs at each tidal gauge are presented in unit meters. MPN, MPO and MPP indicate experiment scenarios for intensified TC with 10% decrement, no adjustment, and 10% increment in translation speed, respectively. OBS represents observed water level data obtained from tidal gauges. The value at the Masan tidal gauge in TC MAEMI (2003) is replaced with hindcast of peak surge height owing to the lack of available data.

	MAEMI (2003)			MAYSAK (2009)			HINNAMNOR (2022)		
	Busan	Masan	Ulsan	Busan	Masan	Ulsan	Busan	Masan	Ulsan
MPN	0.8927	1.7622	0.6241	1.3690	2.3216	0.8670	0.8476	1.4681	0.6253
MPO	0.8594	1.7935	0.6285	1.4297	2.3688	0.9245	0.9155	1.5262	0.6120
MPP	0.8070	1.5984	0.6352	1.3994	2.3144	0.9061	0.9060	1.4667	0.6225
CTL	0.5398	1.2927	0.5351	0.7687	0.8232	0.7861	0.7032	0.8096	0.4974

records the highest surge values overall, reaching up to 2.37 m under the MPO scenario, substantially exceeding the observed peak of 0.82 m. For HINNAMNOR (2022), Masan surge heights vary between 1.47 m and 1.53 m, again exceeding the observed value of 0.81 m. In most storm cases, the MPO scenario generally yields the largest peak surge heights, except for cases in MAEMI (2003) at Busan and HINNAMNOR (2033) at Ulsan. This trend is most pronounced for MAYSAK (2009), where MPO surges exceed those of MPN and MPP at all three gauges.

4. Discussion

A coherent characteristic is evident in that the highest peak storm surge height across both the simulations and observations consistently occurs at the Masan tidal gauge. This tendency is largely attributable to the geographical configuration, where Masan is featured by a semi-enclosed bay with a narrow opening to the sea, causing the amplification of surge effects and making it particularly sensitive to changes in storm properties.

Storm surge response to the intensity enhancement and the translation speed variation of TC varies among the locations and scenarios. For example, the increase of peak storm surge height in MPO scenarios ranges from 17.5% to 88.5%, while showing the minimum sensitivity at Ulsan. Based on preliminary examinations, it is assumed that surge momentum was not fully transferred to the east coast of KP due to the existence of surrounding geographical islands. In contrast, Masan at which three TCs made landfall displayed the highest vulnerability to TC intensification.

Exceptional peak surge height increment was recorded in MASAK (2009), requiring additional inspection on the results. Meanwhile, surge response inconsistency to TC translation speed variation scenarios throughout scenarios implies the underlying complex dynamics associated with storm track, size, and duration of land friction alongside storm intensity. Highest peak surge height mostly occurred in the MPO scenario, except for MAEMI (2003) at BUSAN and HINNAMNOR (2022) at Ulsan where 2~4% increased surge in the MPN case. This indicates that the decrease in translation speed does not necessarily translate to maximum surge, particularly in complex coastal settings such as SEC of KP. The difference between the highest and lowest peak surge height among translation speed variation scenarios ranges from 2.1% to 12.2%. Overall, the findings emphasize the need for subsequent research that incorporates quantitative examination on diverse factors that affect storm surge energy propagation, particularly for highly vulnerable regions such as Masan. The spatial variability observed among tidal gauges further highlights the importance of site-specific assessments when evaluating storm surge hazards under changing climate conditions.

5. Conclusions

This study investigated the response of storm surge heights along the southeastern coast of KP to intensified TCs under varying translation speed scenarios, with a particular focus on Busan, Masan, and Ulsan. By comparing simulated peak storm surge heights under intensified TC conditions (MPN, MPO, and MPP) with observed values from historical events, the analysis provides

insight into how changes in storm intensity and movement can amplify coastal water levels and exacerbate local vulnerability.

Among the three study sites, Masan exhibits the greatest vulnerability across all storm cases, largely due to its semi-enclosed bay geometry that amplifies surge effects. In contrast, Ulsan shows the lowest sensitivity, likely influenced by coastal and island configurations that limit surge momentum transfer. Peak storm surge heights generally occur under the MPO translation speed scenario, although exceptions indicate that reduced translation speed does not always result in maximum surge, particularly in complex coastal settings. The relatively small differences between translation speed scenarios and the spatial variability across tidal gauges highlight the complex and site-dependent nature of storm surge dynamics.

Overall, these findings emphasize the need for site-specific storm surge assessments and further investigation into the combined effects of storm characteristics and coastal geometry, especially for highly vulnerable regions such as Masan under future climate-driven TC intensification.

6. References

- Bloemendaal, N., Haigh, I. D., de Moel, H., Muis, S., Haarsma, R. J., & Aerts, J. C. (2020). Generation of a global synthetic tropical cyclone hazard dataset using STORM. *Scientific data*, 7(1), 40.
- Choi, Mihee & Kim, Minjung. (2024). Estimating Direct and Indirect Damage to Industrial Facilities from Coastal Flooding: Case of Ulsan, Korea. *Journal of the Korean Society of Hazard Mitigation*, 24(4), 257-265.
- Fang, J., Wahl, T., Fang, J., Sun, X., Kong, F., & Liu, M. (2021). Compound flood potential from storm surge and heavy precipitation in coastal China: dependence, drivers, and impacts. *Hydrology and Earth System Sciences*, 25(8), 4403-4416.
- Gyu, E., Hong, S. J., Kang, N., & Kim, H. S. (2015). Flood damage analysis of coastal urban area considering sea level rise and inundation. In *Proceedings of the Korea Water Resources Association Conference* (pp. 447-447). Korea Water Resources Association.
- Hoshino, S., Esteban, M., Mikami, T., Takagi, H., & Shibayama, T. (2016). Estimation of increase in storm surge damage due to climate change and sea level rise in the Greater Tokyo area. *Natural Hazards*, 80(1), 539-565.
- Irish, J. L., Resio, D. T., & Ratcliff, J. J. (2008). The influence of storm size on hurricane surge. *Journal of Physical Oceanography*, 38(9), 2003-2013.
- Jin, H., Hwang, T., Kim, H. J., Min, B. I., & Lee, W. D. (2024). Storm surge simulations using hypothetical scenarios based on historical typhoons impacting the Korean Peninsula: Analysis of storm surge and overtopping volumes. *Journal of Korea Water Resources Association*, 57(12), 1037-1051.
- Karim, M. F., & Mimura, N. (2008). Impacts of climate change and sea-level rise on cyclonic storm surge floods in Bangladesh. *Global environmental change*, 18(3), 490-500.
- Kim, D. Y., Park, S. H., Woo, S. B., Jeong, K. Y., & Lee, E. I. (2017). Sea level rise and storm surge around the southeastern coast of Korea. *Journal of Coastal Research*, (79), 239-243.
- Kim, H. J., Moon, I. J., & Kim, M. (2020). Statistical prediction of typhoon-induced accumulated rainfall over the Korean Peninsula based on storm and rainfall data. *meteorological applications*, 27(1), e1853.
- Kim, H. J., Hwang, T., Min, B. I., Seo, M., & Lee, W. D. (2025). Assessment of Potential Storm Surge Hazards Using the Probabilistic Synthetic Typhoon Ensemble: The Western Coast Nuclear Power Plant Site in Korea. *Journal of Ocean Engineering and Technology*, 39(5), 512-521.
- Kim, S., Joh, C. H., & Lee, S. (2015). Change of damages and damage areas caused by typhoon in South Korea. *Journal of Climate Research*, 10(2), 121-135.
- Kim, S., Kwon, J. H., Om, J. S., Lee, T., Kim, G., Kim, H., & Heo, J. H. (2023). Increasing extreme flood risk under future climate change scenarios in South Korea. *Weather Clim Extremes* 39: 100552.
- Knapp, K. R., Kruk, M. C., Levinson, D. H., Diamond, H. J., & Neumann, C. J. (2010). The international best track archive for climate stewardship (IBTrACS) unifying tropical cyclone

- data. *Bulletin of the American Meteorological Society*, 91(3), 363-376.
- Knutson, T., Camargo, S. J., Chan, J. C., Emanuel, K., Ho, C. H., Kossin, J., ... & Wu, L. (2020). Tropical cyclones and climate change assessment: Part II: Projected response to anthropogenic warming. *Bulletin of the American Meteorological Society*, 101(3), E303-E322.
- Kurihara, Y., Bender, M. A., & Ross, R. J. (1993). An initialization scheme of hurricane models by vortex specification. *Monthly weather review*, 121(7), 2030-2045.
- Lin, N., Emanuel, K., Oppenheimer, M., & Vanmarcke, E. (2012). Physically based assessment of hurricane surge threat under climate change. *Nature Climate Change*, 2(6), 462-467.
- Luettich Jr, R. A., Westerink, J. J., & Scheffner, N. W. (1992). *ADCIRC: An Advanced Three-Dimensional Circulation Model for Shelves, Coasts, and Estuaries. Report 1. Theory and Methodology of ADCIRC-2DDI and ADCIRC-3DL* (No. CERCTRDRP926).
- NHC, cited 2014c: Storm surge overview.
[Available online
at <http://www.nhc.noaa.gov/surge/>.]
- Rego, J. L., & Li, C. (2009). On the importance of the forward speed of hurricanes in storm surge forecasting: A numerical study. *Geophysical Research Letters*, 36(7).
- Skamarock, W. C., Klemp, J. B., Dudhia, J., Gill, D. O., Liu, Z., Berner, J., ... & Huang, X. Y. (2019). A description of the advanced research WRF version 4. *NCAR tech. note ncar/tn-556+str*, 145(10.5065).
- Terenzi, J., Jorgenson, M. T., & Ely, C. R. (2014). Storm-surge flooding on the Yukon-Kuskokwim delta, Alaska. *Arctic*, 360-374.
- Van Nguyen, H., & Chen, Y. L. (2011). High-resolution initialization and simulations of Typhoon Morakot (2009). *Monthly weather review*, 139(5), 1463-1491.
- Wahl, T., Jain, S., Bender, J., Meyers, S. D., & Luther, M. E. (2015). Increasing risk of compound flooding from storm surge and rainfall for major US cities. *Nature Climate Change*, 5(12), 1093-1097.
- Westerink, J. J., Luettich, R. A., Feyen, J. C., Atkinson, J. H., Dawson, C., Roberts, H. J., ... & Pourtaheri, H. (2008). A basin-to channel-scale unstructured grid hurricane storm surge model applied to southern Louisiana. *Monthly weather review*, 136(3), 833-864.
- Yoo, C., Hong, S. H., Choi, H., & Nam, K. W. (2013). A study on flood area typology using the inundation trace map-a case study of Busan Metropolitan City. *Journal of the Korean Society of Surveying, Geodesy, Photogrammetry and Cartography*, 31(5), 393-400.
- Yoo, S. C., Mun, J. Y., Park, W., Seo, G. H., Gwon, S. J., & Heo, R. (2019). Development of bathymetric data for ocean numerical model using sea-floor topography data: BADA ver. 1. *Journal of Korean Society of Coastal and Ocean Engineers*, 31(3), 146-157.